Roles of phenotypic heterogeneity and microenvironment feedback in early tumor development

Matthew Smart [1], Sidhartha Goyal,[1,2,*] and Anton Zilman[1,2,†]

[1]*Department of Physics, University of Toronto, 60 St George St, Toronto, Ontario M5S 1A7, Canada*
[2]*Institute for Biomedical Engineering, University of Toronto, 164 College St, Toronto, Ontario M5S 3G9, Canada*

The local microenvironment of a tumor plays an important and commonly observed role in cancer development and progression. Dynamic changes in the tissue microenvironment are thought to epigenetically disrupt healthy cellular phenotypes and drive cancer incidence. Despite the experimental work in this area there are no conceptual models to understand the interplay between the epigenetic dysregulation in the microenvironment of early tumors and the appearance of cancer driver mutations. Here, we develop a minimal model of the tissue microenvironment which considers three interacting subpopulations: healthy, phenotypically dysregulated, and mutated cancer cells. Healthy cells can epigenetically (reversibly) transition to the dysregulated phenotype, and from there to the cancer state. The epigenetic transition rates of noncancer cells can be influenced by the number of cancer cells in the microenvironment (termed microenvironment feedback). Our model delineates the regime in which microenvironment feedback accelerates the rate of cancer initiation. In addition, the model shows when and how microenvironment feedback may inhibit cancer progression. We discuss how our framework may provide resolution to some of the puzzling experimental observations of slow cancer progression.

I. INTRODUCTION

Cancer initiation and progression is widely thought to occur through a process referred to as clonal evolution [1,2], whereby clonal subpopulations emerge spontaneously and drive tumor growth. Under this setting, cancer progression is defined by the accumulation of mutations in important genes termed cancer "drivers", with typical tumors exhibiting multiple driver gene aberrations [3]. Some driver genes are now well known (e.g., p53, KRAS), and they are broadly characterized as either tumor suppressors or oncogenes [3]. The primary focus of cancer research has been to characterize the function and regulatory networks of identified driver genes in order to classify cancer subtypes and identify druggable targets [3].

Early models of the stepwise accumulation of mutations in cancer have been successful in describing cancer epidemiology (see the classical work of Armitage and Doll [4], and more recently Refs. [5,6]). However, these works are somewhat restricted to the later stages of progression, relying on clinically observable cancer incidence and cancer-associated death. Contemporary models have focused on the earlier steps of cancer initiation and early progression, considering constraints on the population size including the clonal dynamics of subpopulations carrying different mutations [7–10]. These approaches assume each mutation has a specific effect (i.e., beneficial, deleterious, or neutral) on clonal fitness. Clonal subpopulation dynamics can then be described through a variety of modeling techniques. These and similar approaches

have helped to explain driver mutation acquisition and heterogeneity in clonal subpopulations of evolving tumors.

Recently, the gene-centric view of cancer progression has broadened to accommodate the role of epigenetic changes (i.e., which do not require mutations). Such epigenetic changes may arise concurrently with cancer development or precede it, and can be caused for example by aberrant cell-cell signaling or nonmutagenic carcinogens [11–13]. Along with epigenetic changes in cancer cells, the role of the local microenvironment of developing tumors, which consists of the cellular and noncellular components within and near the tumor, has become a subject of intense scrutiny. Interactions between tumor and nontumor (e.g., stromal, immune) cell types of the microenvironment play an important role at all stages of cancer progression [11,14–17].

Experimental studies support the view that cell types and their relative numbers, especially in the tumor microenvironment, should not be regarded as static (reviewed in Ref. [18]). Rather, the number of tumor, immune, and stromal cells, as well as their function, are dynamically changing throughout all cancer stages, from initiation to metastasis. In more advanced tumors, for example, T cells in the microenvironment can adopt "exhausted" phenotypes [15], and macrophages and fibroblasts can adopt tumor supportive phenotypes [14,16,19]. The frequent and clinically significant reports of cancer-associated fibroblasts (CAFs) has led to recent work using *in vitro* populations of nonsmall cell lung cancer cells which investigates how the microenvironment composition (including the presence or absence of CAFs) controls the type of eco-evolutionary game being played [20]. Several related works have investigated the role that tumor microenvironment interactions have on cancer progression in other contexts [21–23]. The biological interactions between microenvironmental sub-

---

*Corresponding author: goyal@physics.utoronto.ca
†Corresponding author: zilmana@physics.utoronto.ca

populations are mediated in part by cell-cell signaling. In addition to classical paracrine signaling pathways, exosomes, cell secreted nanovesicles capable of shuttling internal elements such as RNA between cells, have been recently identified as key mediators of cell type disturbances in the tumor microenvironment ([24–26], reviewed in Refs. [27,28]).

The phenotypic transitions seen in noncancer cells of the microenvironment can occur in the absence of genetic mutations [17,29,30]. At the same time, accumulation of cancer driver mutations in tumor cells is a fundamental hallmark of cancer progression. The question of how the phenotypic dynamics interacts with and modulates mutation accumulation during cancer initiation remains open. This question is closely related to the remarkable prevalence of age-related "indolent" pre-cancerous lesions found in healthy adults [31] (or upon autopsy following noncancer cause of death) [32,33], leading one to question why clinical manifestations of cancer are not more common than observed. These observations have led to a hypothesis that, in addition to the tumor promoting roles outlined above, the microenvironment can also play a role in restraining cancer progression [34].

To address these puzzling observations and clarify the early steps of cancer initiation, we consider a simplified model of the tissue microenvironment involving three interacting subpopulations: healthy, dysregulated, and cancer cells. Healthy cells can epigenetically (reversibly) transition to the dysregulated phenotype, and from there to the cancer state. The epigenetic transition rates of noncancer cells can be influenced by cancer cells in the microenvironment (e.g., through aberrant paracrine signaling). We refer to this as "microenvironment feedback". We focus on a scenario where the intermediate, dysregulated state is a mutator phenotype [35], and the cancer cells are defined as having a driver mutation. The framework is also applicable to more general stepwise scenarios, such as the common metaplasia-dysplasia sequence of cancer progression [36]. Our model extends previous work on the stepwise accumulation of mutations in cell lineages such as Ref. [9], by considering reversibility and microenvironment feedback on the epigenetic transition rates. Deterministically, we find four distinct regimes of the cellular composition in the microenvironment. These regimes include one which represents healthy, cancer-free tissue, another in which the entire population has acquired cancer driver mutations, and two intermediate regimes. With the structure of these regimes characterized, we investigate their implications for cancer initiation by studying the mean time for a clonal subpopulation with two driver mutations to arise, a minimal proxy for cancer initiation [3]. We find that positive microenvironment feedback can be a primary driver of the rate of cancer progression on the one hand and, surprisingly, potentially slow it down depending on the relative division rates of the healthy, dysregulated, and mutated cells. Our results explain how microenvironment feedback can support or inhibit cancer progression in different situations. Finally, we will discuss how the model sheds light on the dynamics of cancer initiation.

II. MODEL

A. Outline of the model

Two fundamental characteristics of cancer initiation are the phenotypic transitions in noncancer cells of the local mi-

croenvironment (which can occur in the absence of genetic mutations), and accumulation of driver mutations in cancer cells. To bridge these two concepts, we treat cell type dysregulation as an intermediate step in cancer establishment and progression, whereby perturbed cells transition to the cancerous states with increased mutation rates. Mutagenicity can be indirectly mediated, for example, by stable downregulation of p53, or directly mediated through elevated expression of mutagenic elements, such as the APOBEC family of proteins [37,38]; microenvironmental mutagenicity has been established in the context of hypoxia and chronic inflammatory settings [39,40]. Furthermore, as the number of cells with driver mutations accumulates, cell signaling is increasingly dysregulated, creating a positive feedback on the system ("microenvironment feedback", see Fig. 1).

We capture these features in a minimal model of three microenvironment subpopulations: x, cells in healthy states; y, cells in the mutator state; and z, cells which have acquired an irreversible cancer driver mutation. To focus the analysis on epigenetic switching and microenvironment feedback, we assume the rate at which the healthy cells x acquire cancer mutations is much smaller than the rate at which the mutator cells y acquire cancer mutations. We denote the division rate of each class of cell by a, b, c, respectively, as shown in Fig. 1. In this paper, we are focusing on the early stage cancer development (pre-cancerous metaplasia and dysplasia) [36], where the relative numbers of each cell type are abnormal but there is no net expansion of the total population. To enforce homeostatic tissue size constraints, we assume that the total population is constant and dynamically conserved, $N \equiv x + y + z$. The qualitative features of our analysis are not changed by relaxing this assumption, see Appendix B.

To summarize, our population dynamics model accounts for state transitions, growth, and population-regulating cell death. The mean-field dynamics of the system are given by

$$\dot{x} = ax - \bar{f}(\mathbf{x})x - \alpha_+ x + \alpha_- y,$$
$$\dot{y} = by - \bar{f}(\mathbf{x})y + \alpha_+ x - \alpha_- y - \mu y,$$
$$\dot{z} = cz - \bar{f}(\mathbf{x})z + \mu y, \tag{1}$$

where the death rate $\bar{f}(\mathbf{x}) = \frac{ax + by + cz}{N}$ enforces fixed population size N. This can be written concisely in vector form,

$$\dot{\mathbf{x}} = (\mathbf{A} + \mathbf{D})\mathbf{x} - \bar{f}(\mathbf{x})\mathbf{x}, \tag{2}$$

where

$$\mathbf{A} = \begin{bmatrix} -\alpha_+ & \alpha_- & 0 \\ \alpha_+ & -\alpha_- - \mu & 0 \\ 0 & \mu & 0 \end{bmatrix}, \quad \mathbf{D} = \begin{bmatrix} a & 0 & 0 \\ 0 & b & 0 \\ 0 & 0 & c \end{bmatrix}.$$

The matrix $\mathbf{A}$ describes the transition rates between subpopulations, and $\mathbf{D}$ the division rates. μ is the rate of acquiring driver gene mutations by y cells, and α_+ (α_-) denotes the transition rate from x to y (y to x). Note that since the overall population number is conserved, the system is effectively two-dimensional, and trajectories evolve on the positive simplex $\Delta \equiv \{x \geqslant 0, \ y \geqslant 0, \ z \geqslant 0 \mid N = x + y + z\}$ [i.e., the physical region of the $N = x + y + z$ plane, see Fig. 2(d)]. Further, without loss of generality we set $a = 1.0$ throughout;
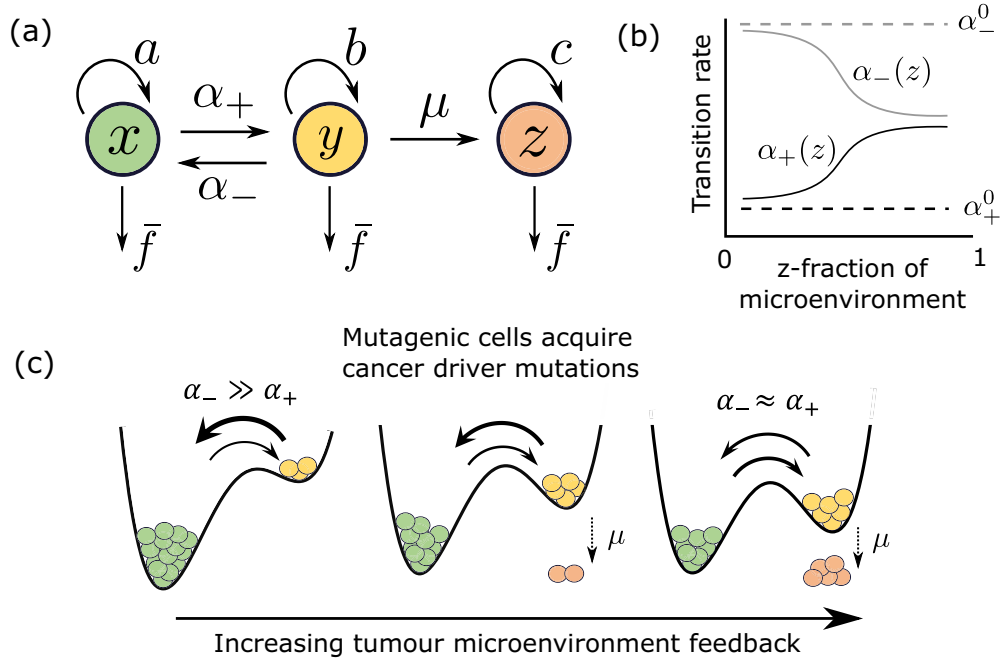
FIG. 1. Model schematic. (a) Birth/death and transition dynamics between cells in healthy states x, mutator states y, and cells with cancer driver mutations z. (b) Incorporating positive feedback from the microenvironment on cell type destabilization. At $z = 0$ the basal rates are α_+^0, α_-^0. When $z \to N$ dysregulation in cell-cell signaling destabilizes normal phenotypes (relative to the mutator ones), as reflected in the model via saturation of $\alpha_+(z)$ to its maximum as $z \to N$, and vice versa for $\alpha_-(z)$. (c) The relative height of two potential wells equalizing reflects the effect of feedback on the transition rates.

timescales are therefore measured in terms of the division rate of healthy x cells.

B. Microenvironment feedback on phenotypic transition rates

As mentioned previously, a major mechanism for cell type destabilization ($x \to y$ transitions) is through dysregulated signaling. Here we assume cells with driver mutations to be the primary source of dysregulated signaling. In a nutshell, we assume that as more cells in a tissue acquire driver mutations, the local signaling in the microenvironment is increasingly dysregulated, further enhancing the cell type destabilization [Figs. 1(b) and 1(c)].

This effective positive feedback is incorporated in the model through z-population-dependent transition rates between the normal x and pathological y cell states [α_+ and α_-, Fig. 1(b)], where increases in number of cancer cells z increases the net rate of epigenetic transitions from x to y [Fig. 1(c)]. We implement this via the following sigmoidal forms:

$$\alpha_+(z) = \alpha_+^0(1 + (\gamma - 1)g(z)),$$

$$\alpha_-(z) = \alpha_-^0\left(1 + \left(\frac{1}{\gamma} - 1\right)g(z)\right), \qquad (3)$$

where $g(z) = \frac{1}{1 + \exp(2\beta(r - z/N))}$ is akin to the Hill function. The results we present are robust to the specific choice of feedback function, see Appendix A 4. Here $\gamma \geqslant 1$ controls the feedback strength, and r, β, are the positive shape parameters (we choose $\beta = 5$, $r = 0.5$ throughout). Note as $z \to 0$, we

have $\alpha_+ \to \alpha_+^0$ and $\alpha_- \to \alpha_-^0$. Conversely, as $z \to N$ we have $\alpha_+ \to \gamma\alpha_+^0$ and $\alpha_- \to \alpha_-^0/\gamma$, stabilizing the mutator state y when feedback is present ($\gamma > 1$).

C. Stochastic description of cancer initiation

In solid tissue, cancer typically begins in small, repeating tissue subunits in which cell growth is tightly regulated [41]. Examples include mammary and pancreatic ducts, liver lobules, and most notably, colon crypts. Such elementary structures have very small population sizes relative to their parent organ. In general, mean-field population dynamics Eq. (1) accurately describe the mean behavior of a large ensemble of such systems; for small system sizes, individual systems may vary significantly from the mean behavior. Understanding this variation is essential to understand the kinetics of cancer progression.

To realize the stochastic description, we consider the master equation $\dot{\mathbf{p}} = \mathbf{M}\mathbf{p}$ associated with our dynamics Eq. (1). Here $\mathbf{p}$ is a vector of occupancy probabilities (i.e. of all possible (x, y, z) states), and $\mathbf{M}$ stores their transition rates [42]. As solving the master equation directly is intractable in this setting, we perform Gillespie simulation [43] to compute stochastic trajectories. In our stochastic analysis we introduce a new absorbing state to our system, $\hat{z}$, which denotes the number of cells with two cancer driver mutations. Two driver mutations are regarded as the minimum required to escape homeostatic control (i.e., tumor growth and malignant progression), and localized tumors are often staged by the presence of multiple driver mutations [3]. Alternative defi-
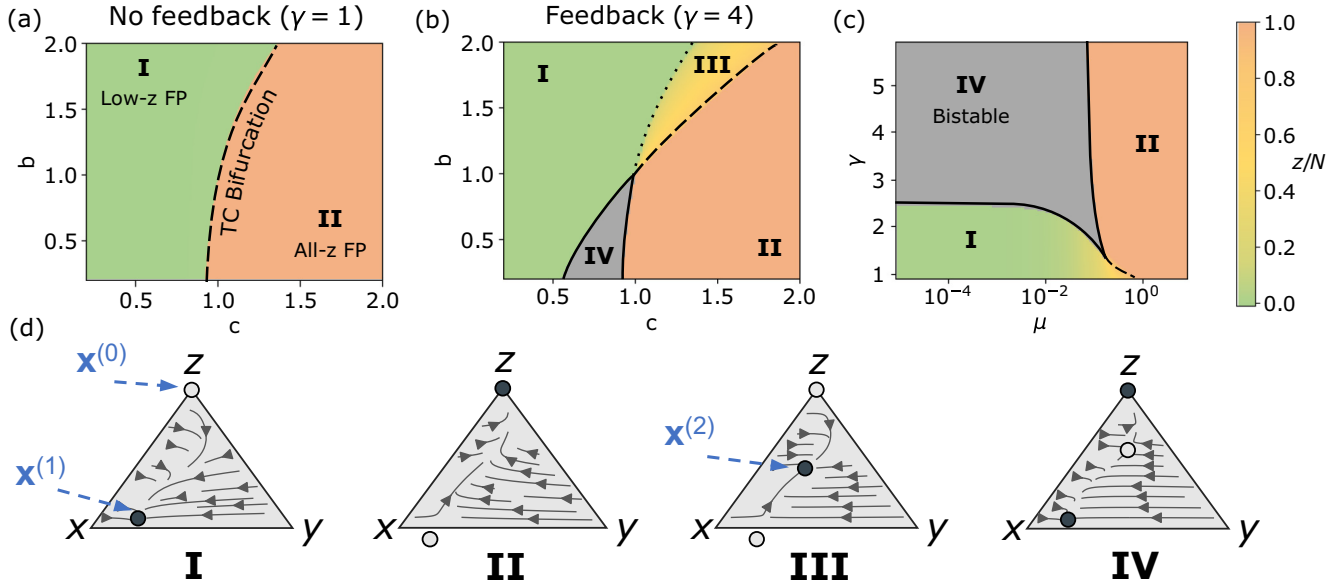
FIG. 2. Deterministic behavior of the model with and without feedback. (a) Without feedback ($\gamma = 1$) the stability diagram has two distinct regions (I, II) defined by the stabilities of the FPs in these regions. For parameters in region I, the system contains a stable "low-z" FP $\mathbf{x}^{(1)}$, and the unstable all-z FP $\mathbf{x}^{(0)}$, as shown in (d). In region II the all-z FP $\mathbf{x}^{(0)}$ is stable and is the only FP in the positive simplex, $\Delta \equiv \{x \geqslant 0, y \geqslant 0, z \geqslant 0 | N = x + y + z\}$ (the unstable FP lies just outside). The two regions are separated by a line of transcritical bifurcations, along which $\mathbf{x}^{(1)}$ approaches $\mathbf{x}^{(0)}$ to exchange stability. (b) Positive feedback (here shown for $\gamma = 4$) leads to the emergence of two additional regimes, III and IV. Region III is similar to region I but the stable FP now has intermediate levels of z cells, and is denoted $\mathbf{x}^{(2)}$. The dashed line separating regions II and III is a transcritical bifurcation as the intermediate FP $\mathbf{x}^{(2)}$ crosses $\mathbf{x}^{(0)}$ to move outside Δ. The dotted line separating regions I and III is a "ghost" of a saddle node bifurcation when $\mu \to 0$ (Appendix A). Region IV is a bistable region where the low-z FP $\mathbf{x}^{(1)}$ and the all-z FP $\mathbf{x}^{(0)}$ are both stable, and the unstable intermediate FP $\mathbf{x}^{(2)}$ splits their basins of attraction. Parameters in (a) and (b): $\alpha_+ = 0.2$, $\alpha_- = 1.0$, $\mu = 10^{-4}$. (c) (μ, γ) cross section of the stability diagram for $\alpha_+ = 0.2$, $\alpha_- = 1.0$, $b = 0.8$, $c = 0.9$. For (a)–(c), color denotes the z fraction of the unique stable FP in both regions. (d) Characteristic flow lines and FP locations (for $\gamma = 4$) for each region, I–IV, are illustrated on Δ. Open dots denote unstable saddle points and solid dots denote stable FPs.

nitions of cancer initiation are possible (e.g., the first *in situ* cancer cell arising during a metaplastic-dysplastic progression – see Discussion). Therefore, to estimate cancer initiation rate as a function of parameters, we study how the distribution of first-passage times (FPTs) to $\hat{z} = 1$ depends on the parameter regime and the initial condition of the system.

III. RESULTS

A. Population dynamics without microenvironment feedback

We first consider the steady state behavior when there is no microenvironment feedback ($\gamma = 1$). Fixed points (FPs) $\mathbf{x}^*$ for the dynamics Eq. (2). are solutions of the steady state condition $\dot{\mathbf{x}} = \mathbf{0}$, i.e.,

$$(\mathbf{A} + \mathbf{D})\mathbf{x}^* = \bar{f}(\mathbf{x}^*)\mathbf{x}^*. \tag{4}$$

The FPs for a given set of parameters are therefore (normalized) eigenvectors of the $\mathbf{A} + \mathbf{D}$ matrix with corresponding eigenvalues $\bar{f}(\mathbf{x}^*)$, implying at most three FPs.

Note that $\mathbf{x}^{(0)} = (0, 0, N)$ is a FP that is independent of model parameters, and it corresponds to every cell having acquired a driver mutation. We refer to this as the "all-z" FP and interpret it as a precancerous state.

As the total population is conserved, we eliminate $z = N - x - y$ to write equations describing equivalent two-

dimensional dynamics on the plane:

$$\dot{x} = \frac{c - a}{N}x^2 + \frac{c - b}{N}xy + (a - c - \alpha_+)x + \alpha_- y,$$
$$\dot{y} = \frac{c - b}{N}y^2 + \frac{c - a}{N}xy + (b - c - \alpha_- - \mu)y + \alpha_+ x. \tag{5}$$

The two other FPs can be found by solving Eq. (5) for $x^* \neq 0$ and $y^* \neq 0$. Only one, $\mathbf{x}^{(1)}$, is possibly physical (i.e., able to lie in Δ). We find that $\mathbf{x}^{(1)}$ is unstable when it is outside Δ, and stable when it is lies in Δ. As $\mathbf{x}^{(1)}$ passes through $\mathbf{x}^{(0)}$ to enter Δ, they exchange stability via a transcritical bifurcation, so that only one of them is stable for a given set of parameters [see Fig. 2(a), regions I and II]. For low μ (the biological scenario which we focus on), $\mathbf{x}^{(1)}$ will typically lie close to the xy edge of Δ when it is stable; we therefore refer to it as the "low-z" FP.

In summary, without feedback there is exactly one biological and stable FP of the dynamics for all biological parameter values. As parameters such as the mutation rate μ or the y, z growth rates are varied, this stable fixed point undergoes a continuous transcritical bifurcation between two regimes: "all-z" ($z^* = N$) and "low-z" ($0 \leqslant z^* < N$), Figs. 2(a) and 2(c). These regimes can be interpreted as pre-cancer and cancer-free states, respectively.

Note that in the limit $\alpha_- \to 0$, the model reduces to the irreversible chain model used in previous works in the

context of mutation accumulation in populations (see, e.g., Refs. [9,44]). In this limit the $x \to y$ transition is effectively irreversible, and so α_+ mathematically can be regarded as a mutation rate to acquire the first "mutation" (the y state), with z now the number of double mutants. Our framework therefore encapsulates previous analysis of the model in the irreversible ($\alpha_- \to 0$) limit and extends it to the more general reversible case. For the case $\alpha_- = 0$, a (b, c) phase diagram has been previously reported [9], with four distinct regions separated by linear bifurcation curves. We find that reversibility simplifies the phase diagram overall, with two instead of four distinct FP topologies separated by a single transcritical bifurcation curve [Fig. 2(a)].

B. Population dynamics with microenvironment feedback

Positive microenvironment feedback leads to a richer phase diagram with four distinct population regions [Figs. 2(b) and 2(c)] denoted as regions I-IV. For low c and a wide range of b (region I), the unique stable FP is dominated by healthy cells (x). As b increases, some of the healthy fraction transitions to the mutator state (y), but the fraction of cells with cancer driver mutations (z) remains very low (moving upwards in region I of Fig. 2(b) causes the corresponding FP [Fig. 2(d)] to move from the bottom-left corner of Δ towards the bottom right).

For high b and increasing c (moving from region I to III), there is a qualitative change where the low-z FP $\mathbf{x}^{(1)}$ moves up to an intermediate-z value, and a third unstable FP moves to lie just below Δ [Fig. 2(d)]. For small but nonzero μ this change is abrupt but does not involve any bifurcations; it is a "ghost" of a saddle node bifurcation which occurs in the limit $\mu \to 0$ (see Appendix A). We therefore denote this intermediate-z FP separately by $\mathbf{x}^{(2)}$. For fixed (b, c), the z coordinate of $\mathbf{x}^{(2)}$ in region III decreases with γ; conversely, the stable FP in region I is qualitatively unchanged by feedback, since z is near zero there.

For low b and increasing c [moving right in Fig. 2(b)], the population switches from a monostable region (I) to a bistable region (IV). In region IV, a low-z FP and $\mathbf{x}^{(0)}$ are both stable, and the intermediate FP $\mathbf{x}^{(2)}$ splits their respective basins of attraction [Fig. 2(d)], region IV). The boundary between IV and II is a line of saddle node bifurcations between the low-z and intermediate FP; if c is increased beyond the boundary, bistability is lost. The boundary between regions I and IV [Fig. 2(b)] is another line of saddle node bifurcations, which meets the right saddle node branch at a cusp. For all biologically relevant values of μ considered in this paper, this boundary effectively overlaps the transcritical line describing stability switching of $\mathbf{x}^{(0)}$ [which separates regions I/IV and II/III in Fig. 2(b)). The region between the two lines expands for large μ and is described in Appendix A. By taking a test point in region IV [e.g., $b = 0.8$, $c = 0.9$, in Fig. 2(b)] and varying μ and γ, we find that the transition from regime I to IV is robust to a wide range of possible values of μ [Fig. 2(c)].

Microenvironment feedback that increases the transition rate into mutator states has several implications for carcinogenesis. As feedback becomes stronger (γ is increased), two conjugate population phases, regions III and IV [Fig. 2(b)], appear. Closer examination of Figs. 2(a) and 2(b) shows

that region III develops within region II whereas region IV develops within region I. This can be understood in the following way: microenvironment feedback can promote cancer progression in situations where the cancer cells and mutator cells divide slowly (region IV); conversely, microenvironment feedback can inhibit cancer progression when mutator cells divide fastest (region III). In addition, we find that feedback allows the all-z, cancer-promoting FP to be stable even when the driver mutation rate μ is orders of magnitude lower than what is needed in the absence of feedback [region IV in Fig. 2(c)] is accessible with feedback at low μ).

C. First-passage time to cancer initiation

As mentioned above, understanding the role of microenvironment feedback on cancer initiation requires a stochastic perspective. We use the FPT to acquire additional cancer driver mutations as a measure of cancer progression, i.e., the FPT to the generation of the first cell with two-driver mutations (we call such cells "double mutants" and denote them by $\hat{z}$) which is typically required for cancer initiation [3]. Other definitions of cancer initiation are possible (e.g., the generation of the first *in situ* cancer cell during a metaplastic-dysplastic progression – see Discussion). We sample the FPT distribution $p(\tau)$ through Gillespie simulation of the master equation of the system Eq. (1) (Sec. II C), starting from the healthy state $x = N$, $y = z = 0$. For simplicity we consider the mutation rate μ from z to $\hat{z}$ to be the same as from y to z.

To focus on the role of the microenvironment, we compare the stochastic dynamics of cancer initiation under (strong) feedback to the no feedback case in regions III and IV (Fig. 2). Note that in the absence of feedback ($\gamma = 1$), region IV becomes region I, and region III becomes region II [Fig. 2(a) and 2(b)]. We find that feedback significantly alters the rate of cancer progression for small populations, due in part to the amplification of fluctuations [42]. As noted elsewhere (e.g., Refs. [9,44]), there are two distinct modes by which a population accumulates mutations: sequential fixation and stochastic tunneling. Both modes are observed in each of the regions we consider. However, we find that sequential fixation is the dominant route in the bistable region IV, as feedback accelerates cancer progression by easing the barrier crossing from the low-z FP to the all-z FP. Stochastic trajectories which reach $z = N$ become trapped until the transition to $\hat{z} = 1$. Conversely, in region III, feedback slows progression by increasing the population fraction of quickly dividing mutator cells ($b > c$, a here), and accordingly lowering the fraction of z. This inhibits stochastic fluctuation to the all-z state, causing the first-passage events to occur at relatively low levels of z (stochastic tunneling). We analyze these cases in more detail in the following subsections.

In our model the mutation rate μ that controls the transition from y to z is much smaller that all the other rates. Due to this separation of time scales the dynamical trajectories of the system rapidly converge onto a "slow" one-dimensional (1D) manifold [shown in a dashed red line in Figs. 3(a) and 3(b)] on the positive simplex, Δ. This slow manifold (SM) connects the slow eigendirections of the stable and unstable FPs [Fig. 2(d)]; mathematically it is a heteroclinic trajectory. Thus, the point in (x, y, z) space from which the first $\hat{z}$ cell ap-
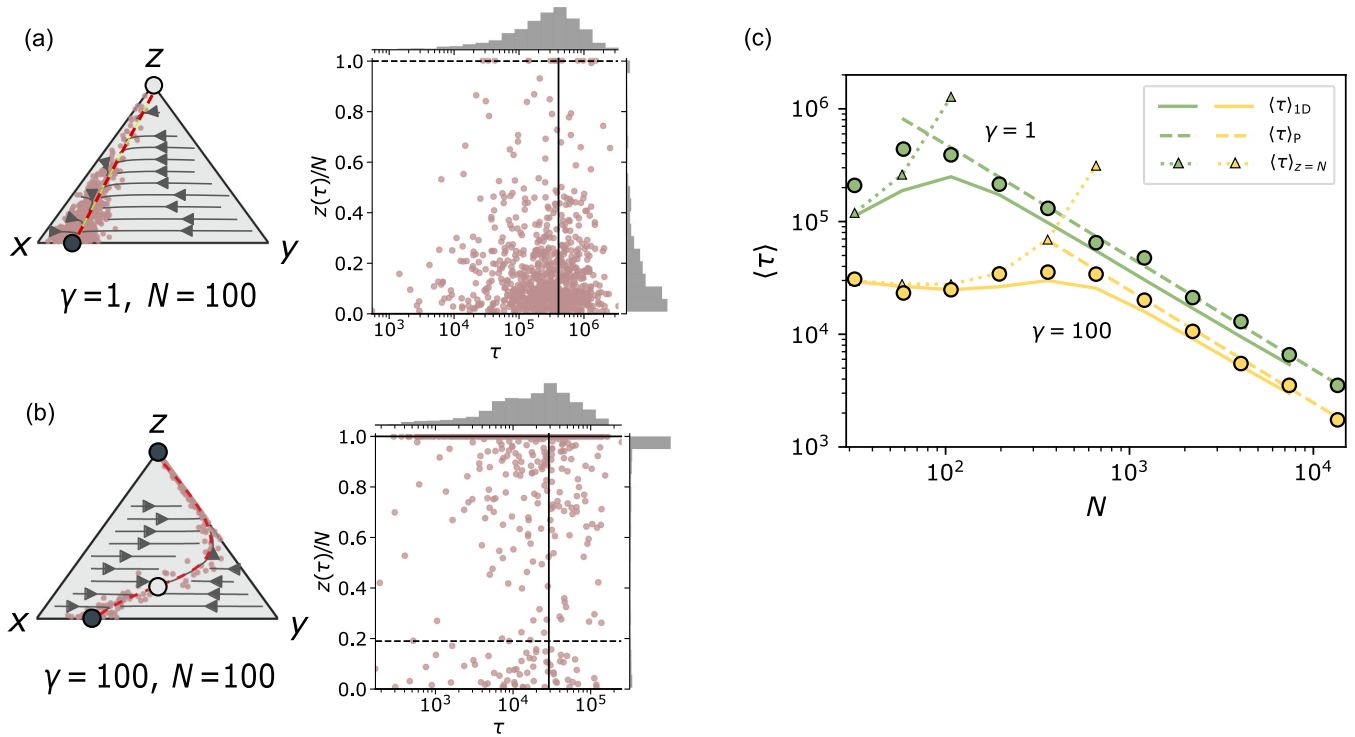
FIG. 3. Analysis of cancer progression rate in regions I and IV. Cancer progression is measured by the FPT, τ, to the first double mutant ($\hat{z} = 1$) for populations starting from the healthy state $x = N$, $y = z = 0$. (a) Results for $N = 100$ and $\gamma = 1$ (region I, which region IV with no feedback becomes). Left: Flow lines and FP locations (black dots) for given parameters and locations of the 800 first-passage events (red dots). The data is concentrated along the slow manifold (SM), which connects the slow eigenvectors of the FPs (shown as red dashed line). Right: The same first-passage events are shown as a joint distribution of τ and the $z(\tau)/N$ at which the event occurred; solid vertical line denotes the mean $\langle\tau\rangle$, the horizontal lines denote stable (solid) and unstable (dashed) FP coordinates. (b) Corresponding results for $N = 100$ and $\gamma = 100$ (region IV; strong feedback). The bulk of the events occur from $z = N$. (c) Mean FPT as a function of N for no feedback, $\gamma = 1$ (green) and strong feedback, $\gamma = 100$ (yellow). Circles denote means of simulated data (240 samples per point). Solid line denotes $\langle\tau\rangle_{1D}$, the approximate MFPT to $\hat{z} = 1$ based on the reduced master equation along the SM (Appendix C). The dashed curve shows $\langle\tau\rangle_P = (\mu z_0)^{-1}$, the rate of $\hat{z}$ cell production from the low-z FP. The dotted curve shows $\langle\tau\rangle_{z=N}$, the time to cross the barrier and reach the fixation point $z = N$. Note $\langle\tau\rangle_{z=N}$ diverging as N increases is a byproduct of stochastic fluctuations decreasing sharply with N. In all panels: $b = 0.8$, $c = 0.9$, $\alpha_+ = 0.2$, $\alpha_- = 1.0$, $\mu = 10^{-4}$.

pears typically lies along this manifold as shown in Figs. 3(a) and 3(b). Accordingly, we can approximate the stochastic dynamics of the system using a 1D master equation $\dot{\mathbf{p}} = \mathbf{W}\mathbf{p}$ for transitions in z along the manifold (see Appendix C). The vector of mean FPTs (MFPT) to $\hat{z}$ from all possible starting conditions, $\boldsymbol{\tau}$, is described by $-1 = \tilde{\mathbf{W}}^T\boldsymbol{\tau}$, where the tilde denotes the removal of the absorbing state's column and row [45]. The quantity of interest, which is the MFPT from $z = 0$ to $\hat{z} = 1$, is given by the first component of $\boldsymbol{\tau}$ and is denoted by $\langle\tau\rangle_{1D}$. This 1D description agrees very well with the full stochastic simulations as shown in Figs. 3(c) and 4(d).

1. First-passage time to $\hat{z} = 1$ in region IV

In region IV $c > b$, so that the mutant z divides faster than y, and both are slower than x. Both the all-z and low-z FPs are stable, and a third saddle FP with an intermediate z value lies on the boundary of their basins of attractions, as shown in Figs. 2(d) and 3(b). Removing feedback ($\gamma \to 1$) changes the topology to that of region I, with one stable FP, low-z, and one unstable FP, all-z. We analyze the FPT to $\hat{z} = 1$ for

a wide range of system sizes, both with and without feedback (Fig. 3).

For large system size $N \gtrsim 1/\mu$, the stochastic population trajectories typically quickly move towards the (stable) low-z FP and stay in its close vicinity until producing the first $\hat{z}$ cell. As the population does not first fixate at all-z, the situation is similar to stochastic tunneling [44]. Denoting the z coordinate of the low-z FP by z_0, a population residing there will produce $\hat{z}$ cells with mean rate μz_0, so that the MFPT to $\hat{z} = 1$ is simply $\langle\tau\rangle_P \equiv (\mu z_0)^{-1}$. This estimate is shown in Fig. 3(c) by dashed lines. This simple picture breaks down for very large $N \gg 1/\mu$, and in this regime one needs to consider the possibility of tunneling along the path from $z = 0$ to the low-z FP (discussed in Appendix C).

Stochastic tunneling to $\hat{z} = 1$ from the low-z FP is no longer the dominant mode of cancer progression when $\mu N \ll 1$ because the waiting time to generate a second mutation at the low-z FP becomes very long. In this regime, the system is more likely to first diffuse to and irreversibly fixate in the $z = N$ state. The FPT to this state is dominated by the time to cross the "barrier" between the stable low-z FP and the unstable FP. The unstable FP is located at $z = N$ without
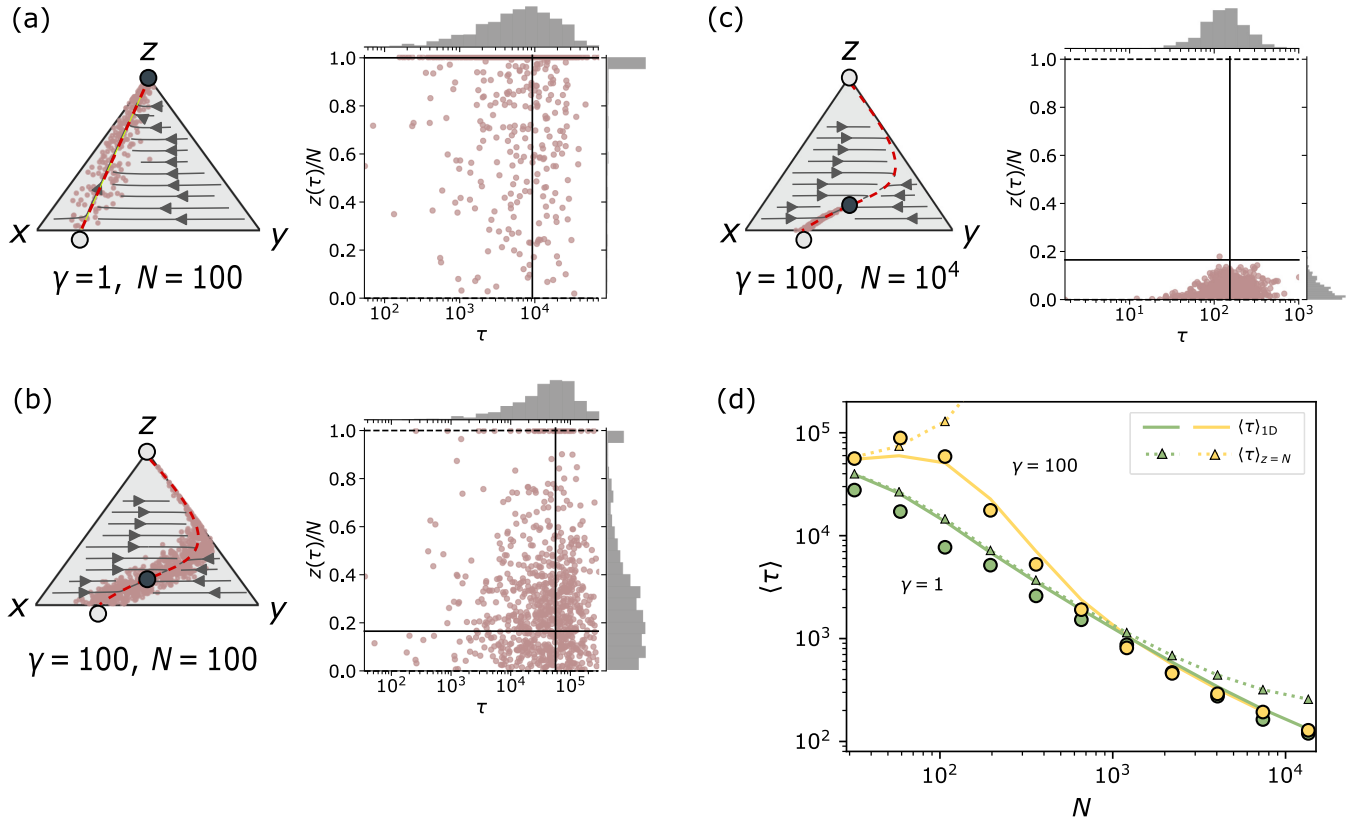
FIG. 4. Analysis of cancer progression rate in regions II and III. Cancer progression is measured by the FPT, τ, to the first double mutant ($\hat{z} = 1$) for populations starting from the healthy state $x = N$, $y = z = 0$. (a) Results for $N = 100$ and $\gamma = 1$ (region II, which region III with no feedback becomes). Left: Flow lines and FP locations (black dots) for given parameters and locations of the 800 first-passage events (red dots). The data is concentrated along the slow manifold (SM), which connects the slow eigenvectors of the FPs (shown as red dashed line). Right: The same first-passage events are shown as a joint distribution of τ and the $z(\tau)/N$ at which the event occurred; solid vertical line denotes the mean $\langle\tau\rangle$, the horizontal lines denote stable (solid) and unstable (dashed) FP coordinates. The majority of the events occur at $z = N$. (b) Corresponding results for $N = 100$ and $\gamma = 100$ (region III; strong feedback). (c) Corresponding results for $N = 10^4$, $\gamma = 100$. (d) Mean FPT as a function of N for no feedback, $\gamma = 1$ (green) and strong feedback, $\gamma = 100$ (yellow). Circles denote means of simulated data (240 samples per point). Solid line denotes $\langle\tau\rangle_{1D}$, the approximate MFPT to $\hat{z} = 1$ based on the reduced master equation along the SM (Appendix C). The dotted triangles shows $\langle\tau\rangle_{z=N}$, the mean time to reach the fixation point $z = N$. In all panels: $b = 1.2$, $c = 1.1$, $\alpha_+ = 0.2$, $\alpha_- = 1.0$, $\mu = 10^{-4}$.

feedback [Fig. 3(a)], and is lowered to an intermediate z value by feedback [see Fig. 3(b)]. In contrast to the stochastic tunneling to $\hat{z} = 1$ state at large N, this scenario is akin to "sequential fixation" where the population first stochastically reaches $z = N$ before producing double mutants with rate μN. In this regime the MFPT from $z = 0$ to $z = N$, denoted as $\langle\tau\rangle_{z=N}$ and shown in Fig. 3(c) as dotted triangles, provides the dominant contribution to the overall cancer initiation time (see Appendix C for details).

As seen in Fig. 3, cancer initiation is faster with feedback (region IV) than without feedback (corresponding portion of region I) for all system sizes. In the stochastic tunneling regime (large N), it has a modest affect, which arises from feedback slightly elevating z_0. In the sequential fixation regime (low N), feedback reduces the MFPT to $\hat{z} = 1$ by making it easier to reach the unstable fixed point because the unstable FP moves from $z = N$ without feedback to an intermediate z value with feedback. This occurs because feedback shifts the $x-y$ balance towards the slowly dividing y cells, which z cells can outcompete in order to climb towards all-z. We show next that feedback has the opposite effect in region III, where the y cells divide quickly.

2. First-passage time to $\hat{z} = 1$ in region III

In region III there is an interior stable FP with an intermediate z value, and the all-z FP is unstable [Figs. 2(d) and 4(b)]. In the absence of feedback ($\gamma = 1$), for the same values of other parameters, the system shifts from region III to region II: the interior FP leaves Δ and the all-z FP becomes stable [Fig. 4(a)]. As in region IV above, due to the separation of time scales between the small mutation rate and other birth, death, and transition rates, the dynamics are mostly constrained to a 1D manifold connecting the slow eigendirections of the FPs (shown by the red dashed line). Hence, also in region III a 1D master equation along this line describes well the MFPT to $\hat{z}$, denoted as $\langle\tau\rangle_{1D}$, from the healthy state $x = N$, $y = z = 0$ [solid lines overlaid on simulation points in Fig. 4(d)].

Without feedback [Fig. 4(a), green curves in Fig. 4(d)], the intermediate stable FP is absent, and for $N \lesssim 1/\mu = 10^4$ the MFPT to $\hat{z}$ from the healthy state is dominated by the MFPT to the all-z FP. This time, denoted $\langle\tau\rangle_{z=N}$ and shown by green triangles in Fig. 4(d), closely agrees with the simulations and $\langle\tau\rangle_{1D}$. Thus, fixation at $z = N$ typically occurs before the first $\hat{z}$ appears [as demonstrated in Fig. 4(a)], so that the first $\hat{z}$

emerges predominantly via sequential fixation. For very large $N \gtrsim 10^4$ the mode switches to stochastic tunneling en route to the FP (see Appendix C).

With feedback [Figs. 4(b) and 4(c), and yellow curves in Fig. 4(d)], these scenarios of cancer initiation become more complex. For very large $N \gtrsim 10^4$ the predominant mode is still stochastic tunneling events concentrated along the SM as shown in Fig. 4(c). For intermediate system size $10^2 \lesssim N \lesssim 10^4$, first-passage events occur throughout Δ [as shown in Fig. 4(b)], but the population rarely fixates at $z = N$ and can also be categorized as a stochastic tunneling scenario. A heuristic for this regime is discussed in Appendix C. For $N \lesssim 10^2$, $\langle \tau \rangle$ follows $\langle \tau \rangle_{z=N}$, the MFPT to fixate at $z = N$, suggesting sequential fixation as the main process.

Taken together, in region III $\langle \tau \rangle$ shows a surprising trend where, unlike region IV, positive feedback slows down the transition rate to $\hat{z} = 1$ as shown by the increase in MFPT in Fig. 4(d) at low N. With feedback, the stable all-z FP comes into the simplex, and by virtue of being a stable FP, creates a sink for fluctuating trajectories. This sink traps and slows the stochastic fixation to all-z state, ultimately increasing the MFPT to the double mutant state.

Analysis of the first-passage time to acquire a second driver mutation indicates how microenvironment feedback can dramatically accelerate or inhibit the rate of cancer initiation. Specifically, we find that in the bistable region (IV), feedback acts to reduce the mean first-passage time for small populations ($N \lesssim 10^3$). Conversely, for region III, we find that feedback increases the mean first-passage time, also in the small population region. For microenvironment populations situated in regions I and II far from the boundary lines (i.e., significant differences between the division rates b, c), feedback does not have a strong effect on the rate of cancer progression. In the next section, we provide estimates of the cancer initiation times and discuss the implication for human cancers.

IV. DISCUSSION

Analysis of the minimal population dynamics model reveals how positive feedback from dysregulated signaling in the microenvironment influences cancer progression. Intuitively, signaling which biases normal cells into an abnormal mutator phenotype should enhance cancer development and progression. Our model and analysis clarify the circumstances and the route by which this feedback enhances cancer progression, and situations where it does the reverse. Although we have focused on a reversible mutator phenotype as the intermediate state in our model, our results are also applicable to more generic stepwise progressions, such as the metaplasia-dysplasia sequence of cancer initiation [36].

Our analysis shows that the positive feedback from the microenvironment provides two key supporting aspects for cancer development. First, by promoting the conversion of healthy cells into mutator phenotypes, feedback allows cells with cancer driver mutations to dominate the total population even if they divide much slower than healthy cells. This contrasts with an assumption in cancer population dynamics that for cancer cells to (deterministically) dominate the total population they must be more fit (divide faster or die less) than

noncancerous cells. In addition, stochastically the positive feedback allows slowly dividing cells with driver mutations to fixate at a rate that is an order of magnitude faster than in the absence of positive feedback [Fig. 3(c)]. Together, these results indicate that decreasing feedback by blocking the positive feedback from the local microenvironment may inhibit cancer development in situations where both the mutator and mutated cells divide slower than normal cells.

Interestingly, microenvironment feedback can inhibit cancer initiation when the mutator cells divide more quickly than mutant cells. This occurs because feedback enhances the transition from healthy to mutator cells, which (due to their faster division rate) then outcompete mutant cells. In this regime, microenvironment feedback can slow the rate of cancer progression by an order of magnitude for small populations by pushing the stochastic dynamics into the tunneling regime (Fig. 4). This may offer a potential explanation for observations of slow cancer progression in some tissues [34], as well as observations of cells with mutations (across many genes, including cancer drivers) present in otherwise healthy tissues without progressing into full blown tumors [46,47]. With respect to impeding cancer initiation, our model suggests that increasing the division rate of mutator cells by chemical agents or therapeutics can be a viable strategy when the mutated cells cannot be targeted directly.

The analysis of our model points to specific strategies for stalling cancer initiation in different regimes. However, these depend on the knowledge of the relative growth rates of healthy, mutator and mutant cell types, which may not be generally accessible. In cases where the tumor has been characterized and treated via traditional therapies, it may be kept in check via the above-mentioned strategies.

By considering physiological values of the model parameters, we may obtain numerical estimates for the calculated MFPTs. We have assumed $\mu = 10^{-4}$ as the rate of driver mutations per cell division in the mutator state (similar to the value used in Ref. [48]). Depending on the tissue and cell type a mammalian cell division rate can be up to $a = 1/\text{day}$ [5,49]. This sets the units of time in our model (in Sec. II we rescale all rates by the division rate or healthy cells, a). Thus, the low-N MFPT with feedback in region IV [Fig. 3(c)] of $\langle \tau \rangle \sim 10^4$ corresponds to ~50 years—a biologically realistic timescale for cancer initiation. Interestingly, when feedback is removed the MFPT $\langle \tau \rangle$ becomes much longer than a typical human lifespan. On the other hand, we observe the opposite effect in region III [Fig. 4(d)]: without feedback $\langle \tau \rangle \lesssim 100$ years, but with strong feedback it takes much longer for cancer to initiate in small populations of cells.

In general, our theory can be compared to data on the frequency of driver mutations in precancerous tissue. Interestingly, the appearance of cells with multiple driver mutations is not on its own sufficient for cancer, as evidenced by the recent observations of cancer driver mutations throughout the somatic tissue of healthy adults [50]. Our model predicts that double mutant lineages will readily appear during a human lifespan in tissues where the microenvironment conditions are favorable. It would be interesting to compare our models predictions with the experimental data on the frequency of somatic driver mutation, including fixation of single driver mutants and the appearance of double mutants as a function

of age, from varying microenvironmental conditions. However, for meaningful comparison to genomic data from human tissue, the model would need to be extended to account for details specific to tissue subtypes, which exhibit different division rates, niche sizes, and typical numbers of driver mutations in the context of cancer initiation. These details will be considered in future work, along with deterministic analysis of the general case of $k > 2$ driver mutations.

A conceptual question in cancer development is how cells accumulate multiple mutations when the first few mutations in a sequence are neutral or deleterious before a final mutation which provides a benefit (as measured by higher proliferation rate) [44], often referred to as crossing a "fitness valley". This scenario is associated with a feed-forward chain, where cells accumulate mutations but rarely revert or lose them [9,44]. In such models, when a cell in the final state divides slower than it would in the initial state, fixation at the final state is deterministically inaccessible, and hence for a small population stochastic sequential fixation is rare. Our model extends this picture, if we interpret the y state as the first mutation and the z state as the second. Due to the two central components of our model: reversibility (the y state can go back to x) and feedback (x to y transition is promoted as more z arise), the all-z state can be deterministically stable despite $c < a$. This stability contributes to the increased rate of cancer progression.

There are several important aspects of our model that may be considered in future work. First, our model treats the microenvironment as spatially homogeneous, whereas developing tumors often display significant heterogeneity [51]. Relaxing this assumption will further clarify the role of the microenvironment in cancer initiation and progression, as suggested in other work [52]. Additionally, we do not explicitly consider the important and complex role of the immune system in the cancer microenvironment [51]. Within the coarse-grained model of the cancer microenvironment we present here, immune regulation may act through modification of the relative fitness of each class of cells. Reduction of c or b relative to the healthy cells may correspond biologically to the immune system suppression of the growth of mutated or epigenetically dysregulated cells. This type of immune regulatory effect could be further investigated in future work by introducing a class of microenvironmental immune cells that affects the relative division rates of each class of cells.

While we have presented the model with a mutation-focused view of cancer in mind, our analysis is also applicable more generally to the development of *in situ* cancer following an accumulation of abnormal cells (metaplasia-dysplasia progression) in the tissue microenvironment [36]. In the context of cancer staging, tissue samples are not simply categorized as "healthy" or "cancer". Rather, there are several early stages identifiable through changes in the tissue architecture (which need not involve mutations). The first step is often cell type switching to a phenotype associated with a different tissue (metaplasia), which is generally considered reversible. Metaplasia may or may not progress to dysplasia, which is considered precancerous and clinically is either closely monitored or treated. In this picture, the y cells are metaplastic and the z cells are dysplastic, with feedback acting to promote metaplastic conversion of the x cells. The rate of dysplastic transition from y to z is potentially much higher than in the

case where the transition requires a mutation. As a result, there is a richer deterministic behavior consisting of two distinct bistable regimes (Appendix A 3). Future work investigating the stochastic behavior for high-μ would therefore involve alternative routes to the fully dysplastic state (or the initial appearance of *in situ* cancer cells), and may help to explain why some metaplasias can progress quickly (e.g., in HPV-associated cancers) [53], while others progress more rarely or slowly (e.g., intestinal metaplasia of the esophagus) [36].

V. MATERIALS AND METHODS

All calculations and simulations were performed in Python 2.7 using NumPy 1.16.2 and SciPy 1.2.2, and Mathematica 10.0. Implementation details of the stochastic simulation are provided in Appendix C.

APPENDIX A: DETERMINISTIC ANALYSIS DETAILS

1. Deterministic analysis without feedback

Special case $\alpha_- \to 0$. Eq. (5) gives the nullcline equations to be solved for nontrivial fixed points $x^*, y^* \neq 0$

$$0 = \frac{c-a}{N}x^2 + \frac{c-b}{N}xy + (a-c-\alpha_+)x,$$

$$0 = \frac{c-b}{N}y^2 + \frac{c-a}{N}xy + (b-c-\mu)y + \alpha_+ x. \quad \text{(A1)}$$

Note if $y^* = 0$, then $x^* = 0$. If $x^* = 0$, one gets $y^*/N = 1 + \mu/(c-b)$. Let $r_1 \equiv c-a+\alpha_+$, $r_2 \equiv c-b+\alpha_-+\mu$, as in the main text. When both $x^*, y^* \neq 0$, solving Eq. (A1) gives the unique nontrivial fixed point:

$$\frac{x^{(+)}}{N} = \frac{r_1(r_1 - r_2)}{r_1(r_1 - r_2 + \alpha_+) - \alpha_+\mu},$$

$$\frac{y^{(+)}}{N} = \frac{\alpha_+ r_1}{r_1(r_1 - r_2 + \alpha_+) - \alpha_+\mu}. \quad \text{(A2)}$$

General case. To identify fixed points besides $\mathbf{x}^{(0)} = (0, 0, N)$, suppose $\mathbf{x}^* = (x^*, y^*, z^*) \neq \mathbf{x}^{(0)}$. Then from Eq. (5), both $x^* \neq 0$ and $y^* \neq 0$ (unless $\alpha_+ = 0$ or $\alpha_- = 0$). Then, at $\mathbf{x}^*$

$$0 = \frac{c-a}{N}x^* + \frac{c-b}{N}y^* + \alpha_- q - r_1,$$

$$0 = \frac{c-b}{N}y^* + \frac{c-a}{N}x^* + \frac{\alpha_+}{q} - r_2. \quad \text{(A3)}$$

This simplifies to a quadratic in q: $0 = \alpha_- q^2 - Rq - \alpha_+$, where $R = r_1 - r_2$. Its two roots determine the nontrivial fixed

points (for $\alpha_+ > 0$, $\alpha_- > 0$). The roots are

$$q_\pm = \frac{1}{2\alpha_-}[R \pm \sqrt{R^2 + 4\alpha_-\alpha_+}]. \tag{A4}$$

Denote the associated fixed points by $\mathbf{x}^{(+)}$, $\mathbf{x}^{(-)}$. Notice q_+, q_- are always real, q_+ is always positive, and q_- is always negative. Thus, $\mathbf{x}^{(-)}$ cannot lie in Δ, but $\mathbf{x}^{(+)}$ possibly can. To express their coordinates, note $\mathbf{x}^{(\pm)} = (x_\pm, \ x_\pm q_\pm, \ N - x_\pm(1 + q_\pm))$, and substitute $q_\pm$ into Eq. (A3) to find

$$\frac{x_\pm}{N} = \frac{-r_1 + \alpha_- q_\pm}{-r_1 + \alpha_+ + (\alpha_- + \mu - r_2)q_\pm}. \tag{A5}$$

Note $\mathbf{x}^{(+)}$ will lie in Δ when $0 < x_+(1 + q_+) < N$. We refer to this this fixed point as the "low-z" state (when it is stable we will generally have $z \ll N$). When $\mathbf{x}^{(+)}$ crosses $\mathbf{x}^{(0)}$ to enter or exit Δ, they exchange stability [Fig. 2(a)]. Further analysis shows that the situation corresponds to a transcritical bifurcation at det $\mathbf{J}(\mathbf{x}^{(0)}) = 0$.

For low-μ, $\mathbf{x}^{(+)}$ will typically lie near the $N = x + y$ edge of Δ when it is stable; we therefore refer to it as the "low-z" FP and interpret it as a healthy state of the tissue. It is denoted as $\mathbf{x}^{(1)}$ in the main text.

The stability of a fixed point can be determined from a local linearization of the dynamics: $\dot{\mathbf{x}} \approx \mathbf{J}(\mathbf{x}^*)(\mathbf{x} - \mathbf{x}^*)$, where $\mathbf{J}(\mathbf{x}^*)$ is the Jacobian of the dynamics evaluated at the point $\mathbf{x}^*$, defined as the matrix of partial derivatives, $J_{ij} = \frac{\partial f_i}{\partial x_j}$ [54]. At $\mathbf{x}^{(0)}$ this gives

$$\mathbf{J}(\mathbf{x}) = \begin{bmatrix} 2\frac{c-a}{N}x + \frac{c-b}{N}y - r_1 & \frac{c-b}{N}x + \alpha_- \\ \frac{c-a}{N}y + \alpha_+ & 2\frac{c-b}{N}y + \frac{c-a}{N}x - r_2 \end{bmatrix}. \tag{A6}$$

A fixed point $\mathbf{x}^*$ is stable if and only if $\mathrm{Re}(\lambda) < 0$ for all eigenvalues λ of $\mathbf{J}(\mathbf{x}^*)$. For 2×2 matrices, this is satisfied when $\mathrm{Tr}\mathbf{J}(\mathbf{x}^*) < 0$ and $\det\mathbf{J}(\mathbf{x}^*) > 0$. For $\mathbf{J}(\mathbf{x}^{(0)})$, this gives the stability criteria

$$\begin{aligned} 0 &< r_1 + r_2, \\ 0 &< r_1 r_2 - \alpha_+\alpha_-, \end{aligned} \tag{A7}$$

where $r_1 \equiv c - a + \alpha_+$, $r_2 \equiv c - b + \alpha_- + \mu$. Together these imply that $\mathbf{x}^{(0)}$ stability requires $r_1, r_2 > 0$. If the class transition rates α_+, α_-, μ are insignificant compared to division rate differences, then Eq. (A7) holds when the cancer cells grow faster than both the healthy and dysregulated cells: $c > \max(a, b)$. If instead the class transition rates are not negligible, then $0 < r_1 r_2 - \alpha_+\alpha_-$ represents a nonlinear balance between mutation and selection that can stabilize the all-z state even when cancer cells grow slower than both the healthy and dysregulated cells.

2. Deterministic analysis with feedback

Recall the reduced dynamics given in Eq. (5) in the main text. To help identify fixed points and bifurcations, consider the coordinate transform $u = \frac{x+y}{N}$, $v = \frac{x-y}{N}$. Since $N = x + y + z$, we can write $z = N(1-u)$. Note u is physical (nonnegative population) only when $u \in [0, 1]$, and v is physical when $v \in [-1, 1]$. At $u = 0$, we have $z = N$ (and $v = 0$, since $x = y = 0$), and at $u = 1$, we have $z = 0$. The feedback factor $g(z)$ controlling α_-, α_+ in Eq. (3) can be written $g(u) = \frac{1}{1+e^{2\beta(-1+r+u)}}$.

The dynamics in the new coordinate system are

$$\dot{u} = \frac{1}{2}(c - a)(u - 1)(u + v) + \frac{1}{2}(u - v)((c - b)(u - 1) - \mu),$$

$$\dot{v} = \frac{1}{2}((c - b)(u - v)(v + 1) + (c - a)(u + v)(v - 1) - 2\alpha_+^0(u + v) + (2\alpha_-^0 + \mu)(u - v))$$

$$+ \frac{\gamma - 1}{\gamma}g(u)(\alpha_-^0(u - v) + \alpha_+^0\gamma(u + v)). \tag{A8}$$

While this might appear less simple than Eq. (5), a single variable FP equation can be derived by first setting $\dot{u} = 0$, which gives an equation for the u nullcline

$$v(u) = \frac{u((2c - b - 1)(1 - u) + \mu)}{(1 - b)(1 - u) + \mu}. \tag{A9}$$

Note that $v(u)$ has an asymptote at $u = 1 + \frac{\mu}{1-b} \approx 1$ which is near the $z = 0$ edge of the simplex. Substituting $v(u)$ into $\dot{v} = 0$ gives the governing equation for FPs $(u^*, \ v(u^*))$

$$0 \equiv F(u) \equiv \frac{2u}{\gamma}\frac{N(u)}{D(u)}, \tag{A10}$$

where we have $D(u) = ((1-b)(1-u) + \mu)^2$, and, writing $G(u) = (g(u) - 1)(\gamma - 1)$,

$$N(u) = G(u)((b - 1)(u - 1) + \mu)((c - 1)(u - 1)\alpha_-^0 + \alpha_+^0\gamma((b - c)(u - 1) + \mu))$$

$$+ \gamma((c - 1)^2(u - 1)((u - 1)(c - b + \alpha_-^0) - \mu) - \alpha_+^0(c + b(u - 1) - cu + \mu)^2$$

$$- (c - 1)(u - 1)((c - b)(u - 1) - \mu)(c - b - \alpha_+^0 + \alpha_-^0 + \mu)).$$

The system therefore always has a FP at $u = 0$, which corresponds to $z = N$. All other FPs are described by $\frac{N(u)}{D(u)}$.

Bifurcations occur when $F(u)$ has a higher-order root. Accordingly, the transcritical (TC) bifurcation curves in Figs. 2(a) and 2(b) can be explained by $N(u)$ having a root at $u = 0$. This occurs when $A_1 G(u) + A_2 = 0$. For $u = 0$, $G(u) \approx 1 - \gamma$. Setting $A_1(\gamma - 1) = A_2$,

$$0 = \alpha_-^0(c-1) + \gamma(c - 1 + \gamma \alpha_+^0)(-b + c + \mu). \quad (A11)$$

This equation describes how feedback augments the stability of the all-z fixed point, and we see that without feedback ($\gamma = 1$) we reidentify the constraint $\det \mathbf{J}(\mathbf{x}^{(0)}) = 0$, Eq. (A7).

The saddle node bifurcations are more complicated but can be recovered analytically in the low-μ approximation.

Low-μ approximation. We assume $\mu \ll 1$ throughout the main text. Here we show that we can analytically describe the low-μ behavior, such as the phase diagram of Fig. 2(b), when we take $\mu \to 0$. This simplifies the FP equation Eq. (A10) as

$$0 = F(u) = \frac{2u}{\gamma(b-1)}(((c-b)(c - 1 + \alpha_+^0) \\ + (c-1)\alpha_-^0)\gamma + G(u)((c-1)\alpha_-^0 + (b-c)\alpha_+^0\gamma)). \\ (A12)$$

From Eq. (A12), three fixed points can be identified:
- $\mathbf{u}^{(0)} \equiv (0,0)$ is the trivial FP of Eq. (A10) which is independent of μ. It corresponds to the all-z FP, $\mathbf{x}^{(0)}$.
- $\mathbf{u}^{(1)} \equiv (1, v^{(1)})$ lies on the line $x + y = N$, $z = 0$. It corresponds to the low-z FP, $\mathbf{x}^{(1)}$, when μ is nonzero. $v^{(1)}$ can be found by solving $\dot{v} = 0$ after substituting $u = 1$.
- $\mathbf{u}^{(2)} \equiv (u^{(2)}, v(u^{(2)}))$, which corresponds to the intermediate-z FP, $\mathbf{x}^{(2)}$, and exists only in regions III, IV [see Fig. 2(b)]. We find $u^{(2)}$ below.

The bracketed factor in Eq. (A12) can be solved analytically to give

$$u^{(2)} = 1 - r + \frac{\text{arctanh}(R)}{\beta}, \quad (A13)$$

where

$$R = \frac{-(c-1)\alpha_-^0(1+\gamma) + \gamma(b-c)(2c - 2 + \alpha_+^0 + \alpha_+^0\gamma)}{(\gamma - 1)((c-1)\alpha_-^0 + (b-c)\alpha_+^0\gamma)}. \\ (A14)$$

Note that $u^{(2)}$ is only physical when inside $[0, 1]$, which requires $|R| = \tanh(2.5) \lesssim 1$ (for $\beta = 5$, $r = 0.5$ as used throughout). However, note that $\text{arctanh}(R)$ is only defined for $-1 < R < 1$. This means once $u^{(2)}$ becomes unphysical, it quickly disappears. We find that setting R to either extreme, which corresponds to divergence of $u^{(2)}$, describes the bifurcation lines for the low-μ phase diagrams. For example, in terms of (b, c), setting $R = 1$ gives

$$b^+(c) = c + \alpha_-^0 \frac{c-1}{c - 1 + \alpha_+^0}, \quad (A15)$$

which we note is independent of feedback. The conjugate curve, found by setting $R = -1$, is

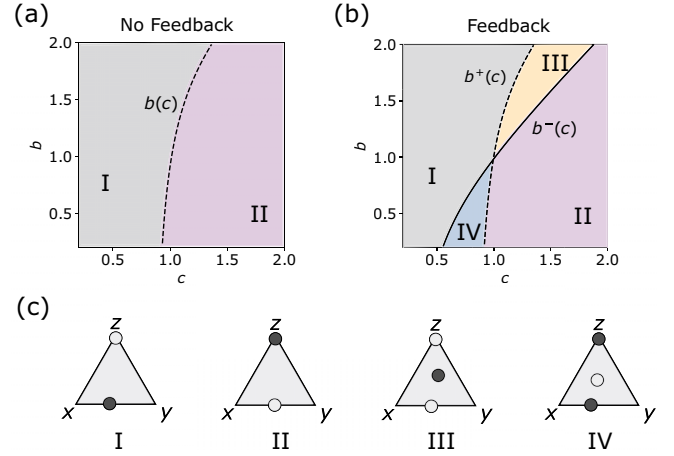$$b^-(c) = c + \alpha_-^0 \frac{c-1}{\gamma(c - 1 + \gamma \alpha_+^0)}. \quad (A16)$$

FIG. 5. Deterministic analysis for $\mu \to 0$. In the low-μ approximation, the bifurcation lines in the main text can be described analytically. (a) When $\gamma = 1$, a line of transcritical bifurcations, described by $b^-(c)$ [which coincides with $b^+(c)$], separates two regions which are analogous to region I and II from the main text. (b) In the presence of feedback, $b^-(c)$ separates from $b^+(c)$, and two regions in which $-1 < R < 1$ open, allowing $\mathbf{u}^{(2)}$ existence. The upper region, which approximates region III, is where $\mathbf{u}^{(2)}$ exists and is stable. In the lower region, which approximates region IV, $\mathbf{u}^{(2)}$ exists and is unstable. (c) FP structure in each region on the $N = x + y + z$ simplex. Solid (open) dot denotes stable (unstable) FP. The upper FP, $\mathbf{u}^{(0)} = (0, 1)$, corresponds to $\mathbf{x}^{(0)} = (0, 0, N)$ ("all z") in the main text. The bottom FP, $\mathbf{u}^{(1)} = (1, v^{(1)})$, is restricted to the xy edge of the simplex and approximates the low-z FP. The intermediate FP, $\mathbf{u}^{(2)}$, with coordinates determined by Eq. (A13), exists only in regions III, IV. Parameters are as in Fig. 2 of the main text.

Notably, these curves coincide in the absence of feedback ($\gamma = 1$). In Fig. 5(a), we observe that $b^-(c)$ captures the transcritical bifurcation curve in Figs. 2(a) and 2(b), and agrees with Eq. (A11) (when $\mu = 0$). With feedback, $b^-(c)$ separates from $b^+(c)$, and two regions in which $-1 < R < 1$ open, allowing $\mathbf{u}^{(2)}$ existence. To deduce the stability of $\mathbf{u}^{(2)}$, we note it must be opposite $\mathbf{u}^{(0)}$ stability [determined by Eq. (A7)]. From Fig. 5(b), it is apparent that $b^+(c)$, $b^-(c)$ describe the bifurcation lines from Fig. 2(b), including the saddle node curves and their "ghost", which have a simple interpretation in the $\mu = 0$ limit. The curve separating regions I/III and IV/II is given by $b^-(c)$ and denotes stability exchange (transcritical bifurcations) between $\mathbf{u}^{(2)}$ and $\mathbf{u}^{(1)}$. The other line, $b^-(c)$, accounts for stability exchange between $\mathbf{u}^{(2)}$ and $\mathbf{u}^{(0)}$.

3. (b, c) phase diagram for high-μ

A high-μ version of Fig. 2(b) in the main text is shown in Fig. 6, with distinct FP regions denoted by color. Figure 6 reveals the transition that occurs on the left edge of the bistable region in Fig. 2(b) (boundary between region I, IV) to in fact be two separate bifurcations that are infinitesimally close as $\mu \to 0$: when c is increased for low b, the system first undergoes a saddle node bifurcation, then a transcritical bifurcation.

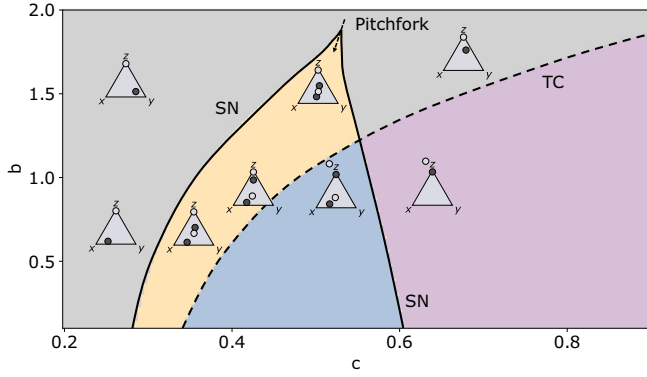FIG. 6. Deterministic analysis in the high-μ case. Phase diagram corresponding to a high-μ ($\mu = 1.0$) extension of Fig. 2(b) of the main text. The triangles represent the positive simplex $N = x + y + z$ with solid (open) circles representing stable (unstable) fixed point (FP) locations. Solid lines denote saddle node (SN) bifurcations along which two FPs are created or destroyed. Dashed line denotes transcritical (TC) bifurcations, corresponding to the all-z FP exchanging stability with another FP. The two SN branches meet at a point representing a pitchfork bifurcation occurring along the dashed arrow. Note the yellow region, exposed here, becomes infinitesimally thin when $\mu \to 0$ as in Fig. 2(b) of the main text. Parameters $\gamma = 4$, $\alpha_+^0 = 0.2$, $\alpha_-^0 = 1$.

4. Alternate functional forms for microenvironment feedback

In the main text we used the simple logistic function $g(z) = \frac{1}{1 + \exp(2\beta(r - z/N))}$ to introduce microenvironment feedback on the epigenetic transition rates in Eq. (3). Here we show that our deterministic results are robust to the particular choice of sigmoidal function.

A widely used function in biological modeling is the Hill function,

$$h(z) = \frac{\left(\frac{z}{N}\right)^n}{r^n + \left(\frac{z}{N}\right)^n},$$

where the Hill coefficient n and controls the strength of the nonlinearity, and r positions the inflection point for large n [Fig. 7(a)].

In Fig. 7, we show (b, c) phase diagrams similar to Fig. 2(b) in the main text. Figure 7(b) uses a Hill coefficient of 1, and Fig. 7(c) uses a Hill coefficient of 2. The plots have minor quantitative differences (note the more gradual transition from region I to III when $n = 1$). Both plots exhibit the four distinct population regions discussed in the main text.

APPENDIX B: DYNAMICS WITH EXPONENTIAL GROWTH

As a relaxation of our model, we consider removing the population fixing death rate term $\bar{f}(\mathbf{x}) = \frac{ax+by+cz}{N}$. The revised dynamics are

$$\dot{\mathbf{x}} = (\mathbf{A} + \mathbf{D})\mathbf{x}, \tag{B1}$$

where

$$\mathbf{A} = \begin{bmatrix} -\alpha_+ & \alpha_- & 0 \\ \alpha_+ & -\alpha_- - \mu & 0 \\ 0 & \mu & 0 \end{bmatrix}, \quad \mathbf{D} = \begin{bmatrix} a & 0 & 0 \\ 0 & b & 0 \\ 0 & 0 & c \end{bmatrix}.$$

Without feedback, this is a linear system and fixed points correspond to Null($\mathbf{A} + \mathbf{D}$). In general, $\mathbf{A} + \mathbf{D}$ is nonsingular and so the unique fixed point is $\mathbf{x} = \mathbf{0}$, in contrast to the population conservation case.

However, notice if we write $N = x + y + z$, then $\dot{N} = ax + by + cz$, and we can define the dynamics of population fractions $\mathbf{u} \equiv \mathbf{x}/N$ as

$$\dot{u} = (a - \alpha_+)u + \alpha_- v - (au + bv + cw)u,$$
$$\dot{v} = \alpha_+ u + (b - \alpha_- - \mu)v - (au + bv + cw)v,$$
$$\dot{w} = \mu v + cw - (au + bv + cw)w. \tag{B2}$$

This is the same form as our original dynamics with conserved population. Deterministically, this implies the system reaches the same population fractions as it would with the constant population constraint, but now with an unbounded population. However, the stochastic behavior should be quite different when the population is fixed to a low value (e.g., $N = 100$) in the constrained population case.
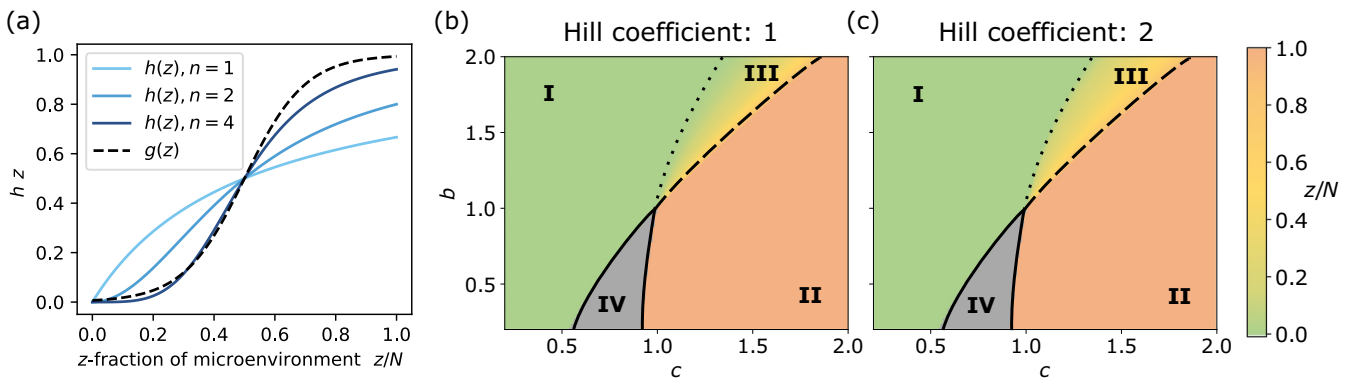

FIG. 7. Robustness of deterministic results to the choice of feedback function. (a) The logistic function $g(z)$ from the main text (with $\beta = 5$, $r = 0.5$) is plotted alongside $h(z)$ with $r = 0.5$ and $n = 1$, 2, and 4. Panels (b) and (c) show phase diagrams consistent with Fig. 2(b) in the main text, which used $g(z)$ to model the feedback (with $\gamma = 4$). In (b) the Hill function $h(z)$ is used with Hill coefficient $n = 1$, and in (c) $n = 2$. Color denotes the z fraction of the stable fixed point. The grey region is bistable as in Fig. 2(b).

APPENDIX C: ANALYSIS OF MEAN FIRST-PASSAGE TIME TO ACQUIRE A SECOND DRIVER MUTATION

1. Specification of the reduced master equation along the slow manifold

The path connecting the slow eigendirections of each fixed point in the vicinity of the simplex defines the slow manifold (SM). Because the birth/death events and epigenetic transitions between x and y are generally much faster than the mutation rate μ, the population has time to quasiequilibrate (in terms of x, y) between each mutation event from y to z. This is reflected in the relative magnitudes of the eigenvalues for the linearized dynamics about the FPs: the eigenvalues whose eigenvectors point along the SM are generally much smaller. This separation of timescales allows one to consider a lower-dimension approximation of the system.

Because the first-passage events (see Figs. 3 and 4 of the main text) concentrate along the SM, we consider a 1D master equation along the SM which tracks transition in z only. To define the manifold, we numerically compute the deterministic trajectory starting from the vicinity of the unstable FP (and combine the segments if necessary).

The 1D master equation for transitions in z along the SM is a $(N + 1) \times (N + 1)$ linear system $\dot{\mathbf{p}} = \mathbf{W}\mathbf{p}$, where the nth component of $\mathbf{p}$ is $p_n(t) = \mathrm{p}(z = n, t)$, and $W_{n,m}$ is the transition rate from $z = m$ to $z = n$. The elements of $\mathbf{W}$ are given by

$$
\begin{aligned}
W_{1,0} &= \mu y(0), \\
W_{z+1,z} &= cz + \mu y(z) \quad \forall \quad z < N, \\
W_{z-1,z} &= \bar{f}(z)z \quad \forall \quad z < N,
\end{aligned}
\tag{C1}
$$

where $0 \leqslant z \leqslant N$. Note $\bar{f}(z) = \bar{f}(x(z), y(z), z)$ is the (population averaged) division rate at coordinate z on the SM. All other off-diagonal elements are 0, and $W_{ii} = -\sum_{j=0}^{N} W_{ji}$ to conserve probability.

The absorbing state of the system defined above is $z = N$. To find the MFPT to $z = N$ from any other state, we only need to perform a matrix inversion ($-1 = \tilde{\mathbf{W}}^T \boldsymbol{\tau}$, where tilde denotes the removal of the absorbing state's column and row), which is very fast when N is not too large ($N \lesssim 10^4$). To further consider the MFPT to $\hat{z}$ (first cell with a second driver mutation), we can append $\hat{z}$ to the system by adding an extra row and column to $\mathbf{W}$:

$$
\begin{aligned}
W_{\hat{z},z} &= \mu z, \\
W_{z,\hat{z}} &= 0,
\end{aligned}
\tag{C2}
$$

for all $0 \leqslant n \leqslant N$. Note that $\hat{z}$ replaces $z = N$ as the sole absorbing state of the system. Solving $-1 = \tilde{\mathbf{W}}^T \boldsymbol{\tau}$ for this extended $\mathbf{W}$ now gives the MFPT vector to $\hat{z}$. In the main text we consider the first element, denoted $\langle \tau \rangle_{1D}$, corresponding to the initial condition $z = 0$.

2. Stochastic tunneling along the deterministic path

For large system size N, stochastic trajectories closely follow the deterministic path $z(t)$ from the healthy state $x = N$ to the associated stable FP. At any instant along the trajectory a double mutant cell can arise, with the rate $\sim \mu z(t)$. Hence, the probability density for the first such event to happen,
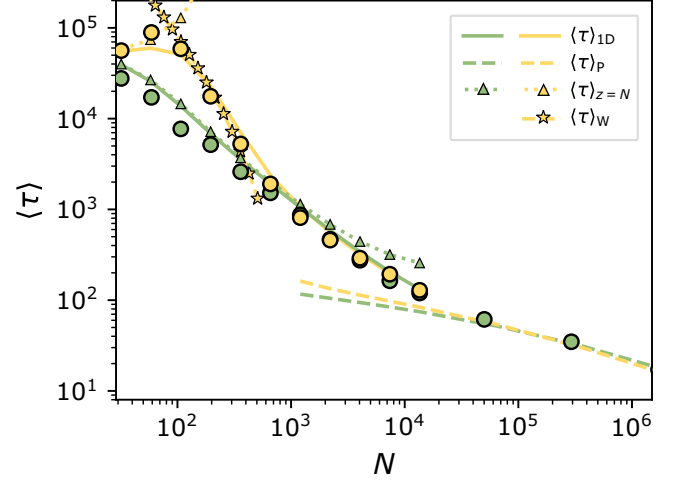

FIG. 8. Heuristic MFPT to $\hat{z} = 1$. MFPT to the first double-mutant, $\hat{z}$, for varying N for no feedback (green) and strong feedback (yellow). Circles denote means of simulated data (240 samples per point), with trajectories starting from the healthy state $x = N$, $y = z = 0$. Solid lines denote $\langle \tau \rangle_{1D}$, the approximate MFPT to $\hat{z}$ based on the reduced master equation along the SM; this closely matches the data up to $N = 10^4$ (not computed beyond due to memory constraints). The triangle dotted curve shows $\langle \tau \rangle_{z=N}$, the MFPT to fixate at $z = N$. The yellow star curve shows $\langle \tau \rangle_W$ for the $\gamma = 100$ case. Dashed lines are the SM path flux $\langle \tau \rangle_P$, valid for large N. Parameters: $b = 1.2$, $c = 1.1$, $\alpha_+ = 0.2$, $\alpha_- = 1.0$, $\mu = 10^{-4}$.

$p_1(t)$, is described by a nonhomogenous Poisson process, $p_1(t) = \mu z(t) e^{-\int_0^t \mu z(\tau) d\tau}$ [55]. The MFPT for these tunneling events which occur along the deterministic path to the FP is given by $\langle \tau \rangle_P \equiv \int t p_1(t) dt$. This describes the behavior for very large $N \gg 1/\mu$ (see Fig. 8).

3. Fokker-Planck expansion of the slow manifold master equation

The Fokker-Planck approximation of a 1D birth-death process such as in Appendix C1 is given by

$$
\frac{\partial p(z, t)}{\partial t} = -\frac{d}{dz}(A(z)p) + \frac{1}{2}\frac{d^2}{dz^2}(B(z)p),
\tag{C3}
$$

where $A(z) = (c - \bar{f}(z))z + \mu y(z)$ is the birth rate minus the death rate, and $B(z) = (c + \bar{f}(z))z + \mu y(z)$ is their sum, see e.g., Ref. [56].

In this representation, analytic approximations of relevant quantities are known, such as the probability of hitting either $z = 0$ or $z = N$ from an intermediate point (treating $z = 0$ and $z = N$ as absorbing boundaries) [56]. The probability to hit $z = N$ first, starting from $z = 1$, is $p_N = \frac{\int_0^1 \psi(z)^{-1} dz}{\int_0^N \psi(z)^{-1} dz}$, where $\psi(z_0) = e^{2\int_0^{z_0} A(z)/B(z)dz}$. We can use p_N to understand the scaling the exact 1D MFPT to reach $z = N$, $\langle \tau \rangle_{z=N}$. Defining the y coordinate at $z = 0$ on the SM by $y_0 \equiv y(0)$, the rate at which attempts are made to reach $z = N$ is μy_0, and they succeed with probability p_N. Thus, the heuristic MFPT to reach $z = N$ is $\langle \tau \rangle_B \equiv \frac{1}{\mu y_0} \times \frac{1}{p_N}$.

In the low-N regime where barrier crossing occurs, $N \ll 1/\mu$, so we can neglect $\mu y(z)$ for $z \neq 0$. The di-

vision rate advantage of z in comparison the population average, $s(z) \equiv c/\bar{f}(z) - 1$, is sufficient to describe stochastic trajectories. Since $|s(z)| \ll 2$, we therefore have $\frac{A(z)}{B(z)} \approx \frac{s(z)}{2}$, so that $\psi(z_0)^{-1} = e^{-\int_0^{z_0} s(z)dz}$. The numerator of p_N is effectively a constant since $s(z)$ varies little from $z = 0$ to $z = 1$, so $\int_0^1 e^{-\int_0^z s(z')dz'} dz \approx e^{-s_0} \sim 1$. Thus, $p_N \approx e^{-s_0}[\int_0^N e^{-\int_0^z s(z')dz'} dz]^{-1}$. The heuristic MFPT to reach $z = N$ is then $\langle \tau \rangle_{\mathrm{B}} \approx \frac{1}{\mu} \frac{e^{s_0}}{(y_0/N)} I(N)$, where $I(N) \equiv \int_0^1 e^{-N\int_0^{\bar{z}} s(\bar{z}')d\bar{z}'} d\bar{z}$, with $\bar{z} \equiv z/N$.

To proceed one needs to consider how $s(z)$ depends on the regime. Without feedback ($\gamma = 1$) it is linear, $s(z) = s_0(1 - z/N)$. Then $\int_0^{\bar{z}} s(\bar{z}')d\bar{z}' = -s_0(\frac{1}{2}\bar{z}^2 - \bar{z})$, and we can evaluate $I(N)$ directly (depending on the sign of s_0). In region I, s_0 is negative, and we get $I(N) = \frac{\sqrt{\frac{\pi}{2}} e^{\frac{|s_0|N}{2}} \mathrm{erf}(\sqrt{\frac{|s_0|N}{2}})}{\sqrt{|s_0|N}}$, which rapidly diverges with N, in agreement with Fig. 3(c). In region II, s_0 is positive, and there we get $I(N) = \frac{\sqrt{\frac{\pi}{2}} e^{-\frac{s_0 N}{2}} \mathrm{erf}(\sqrt{\frac{s_0 N}{2}})}{\sqrt{s_0 N}}$. This behaves like $1/s_0 N$ at large N, in agreement with Fig. 4(d).

With feedback $s(z)$ becomes nonlinear, but we may approximate it using a piecewise linear function with a bend at $s(z_1) = s_1$. For $z \leqslant z_1$: $s_L(\bar{z}) \equiv s_0 + (s_1 - s_0)\frac{\bar{z}}{\bar{z}_1}$, and so $\int_0^{\bar{z}} s_L(\bar{z}')d\bar{z}' = \frac{1}{2\bar{z}_1}(s_1 - s_0)\bar{z}^2 + s_0\bar{z}$. The right branch has the form $s_R(\bar{z}) \equiv s_1 \frac{(1-\bar{z})}{(1-\bar{z}_1)}$, and so for $z \geqslant z_1$,

$$\int_0^{\bar{z}} s(\bar{z}')d\bar{z}' = \int_0^{\bar{z}_1} s_L(\bar{z}')d\bar{z}' + \int_{\bar{z}_1}^{\bar{z}} s_R(\bar{z}')d\bar{z}'$$
$$= \bar{z}_1\left(\frac{s_1 + s_0}{2}\right) + s_1\frac{(\bar{z} - \bar{z}_1)}{(1 - \bar{z}_1)}\left(1 - \frac{\bar{z} + \bar{z}_1}{2}\right).$$

Putting this together, we get $I(N) = I_1 + I_2$, where $I_1(N) = \int_0^{\bar{z}_1} e^{-N(\frac{s_1-s_0}{2\bar{z}_1}\bar{z}^2 + s_0\bar{z})} d\bar{z}$, and $I_2(N) \equiv \int_{\bar{z}_1}^1 e^{-N(s_1\frac{(\bar{z}-\bar{z}_1)}{(1-\bar{z}_1)}(1-\frac{\bar{z}+\bar{z}_1}{2}) + \bar{z}_1(\frac{s_1+s_0}{2}))} d\bar{z}$. The asymptotic behavior of these integrals depends on s_0, s_1. In region IV, $s_0 < 0$, $s_1 > 0$, so that for large N we have $I_2(N) \approx 0$ and $I(N) \approx I_1(N) = \sqrt{\frac{\pi C}{N}} e^{s_0^2 C^2 N}(\mathrm{erf}(|s_0|C\sqrt{N}) + \mathrm{erf}(s_1 C\sqrt{N}))$, where $C(\gamma) \equiv \sqrt{\frac{\bar{z}_1}{2(s_1-s_0)}}$. Feedback decreases $\bar{z}_1$ and increases s_1, the maximum selective advantage of z cells. Note when $\bar{z}_1 \to 1$ and $s_1 \to 0$ this expression reduces to the no feedback case with $C_{\gamma=1} = \frac{1}{\sqrt{2|s_0|}}$. For large N, $I(N) \approx 2\sqrt{\frac{\pi C}{N}} e^{s_0^2 C^2 N}$, and since $C(\gamma)$ becomes smaller with γ, this explains the MFPT speedup (with

feedback) observed in Fig. 3(c). In region III we instead have $s_0 > 0$, $s_1 < 0$, so that asymptotically, $I_1(N) \approx 0$ and

$$I(N) = I_2(N) = \sqrt{\frac{\pi(1-\bar{z}_1)}{2N|s_1|}} e^{N\frac{|s_1|}{1-\bar{z}_1}(\bar{z}_1 - \frac{s_1^2+1}{2})} \mathrm{erfi}(\sqrt{N(1 - \bar{z}_1)|s_1|}).$$

Note also that $|s_1|$ increases with feedback. For large N, $I(N) \sim \frac{1}{\sqrt{2}|s_1|N} e^{(1-\bar{z}_1)|s_1|N}$. Thus, $I(N)$ explains the divergence of $\langle \tau \rangle_{z=N}$ for $\gamma = 100$ in Fig. 4(d).

4. Heuristic mean first-passage time in region III

Here we present heuristics which explain the overall behavior of the MFPT to $\hat{z}$ in region III [Fig. 4(d)] in the main text). In Fig. 8, we provide a more detailed description of Fig. 4(d).

Like region IV, here there are two regimes whose boundary $\mu N \sim 1$ is determined by the rate at which mutants can arise and population size. In the large population regime, $\mu N \gg 1$, as the population flows to the stable FP, first-passage events (to $\hat{z} = 1$) occur en route, and $\langle \tau \rangle_{\mathrm{P}}$ describes the MFPT (see Appendix C 2.; dashed line in Fig. 8); in the low population regime where stochastic effects become more prominent, $\langle \tau \rangle_{\mathrm{P}}$ underestimates the MFPT. However, unlike region IV, feedback now slows down the transition rate to the double mutant state.

For low population sizes, the population quickly quasiequilibrates on the $z = 0$ edge of the simplex, along the stable axis of the saddle FP that lies just below [Figs. 4(a) and 4(c)]. A single mutant is then stochastically generated at rate μy_0. The fate of this z cell is determined by the birth-death dynamics along the 1D manifold, described by $s(z) \equiv c/\bar{f}(z) - 1$ (as discussed above). In this case $s(z) > 0$ and early stochastic dynamics is "selective" but as z increases towards the stable FP in the interior $s(z) \to 0$ and the dynamics becomes "neutral". Since each z-cell lineage starts with one cell its early dynamics is stochastic and many of the lineages go "extinct" (and the system goes back to the $z = 0$ state).

Neutral regime $\langle \tau \rangle_W$. Here we want to compute the probability of getting a double mutant before a lineage fixates. For a lineage which fails to fixate (i.e., eventually returns to $z = 0$), the chance that a double mutant arises in the *window* of time before it goes extinct is a function of the area under the curve $A(T) = \int_0^T z(t)dt$ with boundary conditions $z(0) = 1$ and $z(T) = 0$, where T is the average length of a lineage. Assuming neutral dynamics for a lineage, $A(T) \sim T^2$. Now the probability that a double mutant does not arise during a lineage is given by $p_0 = e^{-\mu T^2}$. Hence, in this regime the MFPT is $\langle \tau \rangle_W \approx \frac{1}{\mu y_0} \times \frac{1}{1-p_0}$. For $s(z) \ll 1$, $T \approx \int_1^N \frac{1}{(1+z)\bar{f}(1+z)} e^{\int_0^z s(z')dz'} dz$ [57]. This heuristic is included in Fig. 8, an extension of Fig. 4(d).

[1] P. C. Nowell, Science **194**, 23 (1976).

[2] M. Greaves and C. C. Maley, Nature (London) **481**, 306 (2012).

[3] B. Vogelstein, N. Papadopoulos, V. E. Velculescu, S. Zhou, L. A. Diaz, and K. W. Kinzler, Science **339**, 1546 (2013).

[4] P. Armitage and R. Doll, Br. J. Cancer **8**, 1 (1954).

[5] P. Calabrese and D. Shibata, BMC Cancer **10**, 3 (2010).

[6] S. A. Frank, Curr. Biol. **14**, 242 (2004).

[7] C. S. O. Attolini and F. Michor, Ann. N. Y. Acad. Sci. **1168**, 23 (2009).

[8] F. Michor, Y. Iwasa, and M. A. Nowak, Nat. Rev. Cancer **4**, 197 (2004).

[9] P. Ashcroft, F. Michor, and T. Galla, Genetics **199**, 1213 (2015).

[10] D. Wodarz, A. C. Newell, and N. L. Komarova, J. R. Soc. Interface **15**, 20170967 (2018).

[11] J. C. Zenklusen et al., Nat. Med. **21**, 846 (2015).

[12] M. B. Yaffe, Sci. Signal. **12**, eaaw3483 (2019).

[13] S. Baker, Br. J. Med. Med. Res. **4**, 1149 (2014).

[14] L. Yang and Y. Zhang, J. Hematol. Oncol. **10**, 58 (2017).

[15] Y. Jiang, Y. Li, and B. Zhu, Cell Death. Dis. **6**, e1792 (2015).

[16] M. Hara, T. Nagasaki, H. Takeyama, H. Takahashi, T. Sato, and K. Shiga, Cancers (Basel) **7**, 2443 (2015).

[17] K. M. Bussard, L. Mutkus, K. Stumpf, C. Gomez-Manzano, and F. C. Marini, Breast Cancer Res. **18**, 1 (2016).

[18] J. Varga and F. R. Greten, Nat. Cell Biol. **19**, 1133 (2017).

[19] V. Koliaraki, C. K. Pallangyo, F. R. Greten, and G. Kollias, Gastroenterology **152**, 964 (2017).

[20] A. Kaznatcheev, J. Peacock, D. Basanta, A. Marusyk, and J. G. Scott, Nat. Ecol. E **3**, 450 (2019).

[21] D. Basanta, J. G. Scott, M. N. Fishman, G. Ayala, S. W. Hayward, and A. R. A. Anderson, Br. J. Cancer **106**, 174 (2012).

[22] A. R. A. Anderson, A. M. Weaver, P. T. Cummings, and V. Quaranta, Cell **127**, 905 (2006).

[23] A. Kaznatcheev, R. Vander Velde, J. G. Scott, and D. Basanta, Br. J. Cancer **116**, 785 (2017).

[24] W. Pang, J. Su, Y. Wang, H. Feng, X. Dai, Y. Yuan, X. Chen, and W. Yao, Cancer Sci. **106**, 1362 (2015).

[25] Z. Y. A. Elmageed et al., Stem Cells **32**, 983 (2014).

[26] A. Hoshino et al., Nature (London) **527**, 329 (2015).

[27] N. Syn, L. Wang, G. Sethi, J. P. Thiery, and B. C. Goh, Trends Pharmacol. Sci. **37**, 606 (2016).

[28] A. O'Loghlen, Philos. Trans. R. Soc. B Biol. Sci. **373**, 20160488 (2018).

[29] D. L. Marks, R. Lo Olson, and M. E. Fernandez-Zapico, Epigenomics **8**, 1671 (2016).

[30] M. Liu, J. Zhou, Z. Chen, and A. S. L. Cheng, J. Pathol. **241**, 10 (2017).

[31] L. J. Esserman et al., Lancet Oncol. **15**, E234 (2014).

[32] H. G. Welch and W. C. Black, Ann. Intern. Med. **127**, 1023 (1997).

[33] A. R. Zlotta et al., J. Natl. Cancer Inst. **105**, 1050 (2013).

[34] M. J. Bissell and W. C. Hines, Nat. Med. **17**, 320 (2011).

[35] L. A. Loeb, Cancer Res. **61**, 3230 (2001).

[36] V. Giroux and A. K. Rustgi, Nat. Rev. Cancer **17**, 594 (2017).

[37] S. A. Roberts and D. A. Gordenin, Nat. Rev. Cancer **14**, 786 (2014).

[38] J. Zou, C. Wang, X. Ma, E. Wang, and G. Peng, Cell Biosci. **7**, 29 (2017).

[39] J. Yuan and P. M. Glazer, Mutat. Res. - Fundam. Mol. Mech. Mutagen. **400**, 439 (1998).

[40] F. Colotta, P. Allavena, A. Sica, C. Garlanda, and A. Mantovani, Carcinogenesis **30**, 1073 (2009).

[41] F. Michor, S. A. Frank, R. M. May, Y. Iwasa, and M. A. Nowak, J. Theor. Biol. **225**, 377 (2003).

[42] N. G. Van Kampen, *Stochastic Processes in Physics and Chemistry*, 3rd edition (North Holland, Amsterdam, 2007), p. 96.

[43] D. T. Gillespie, Annu. Rev. Phys. Chem. **58**, 35 (2006).

[44] D. B. Weissman, M. M. Desai, D. S. Fisher, and M. W. Feldman, Theor. Popul. Biol. **75**, 286 (2009).

[45] S. Iyer-Biswas and A. Zilman, Adv. Chem. Phys. **160**, 261 (2016).

[46] K. Yizhak et al., Science **364**, eaaw0726 (2019).

[47] I. Martincorena et al., Science **348**, 880 (2015).

[48] I. Bozic et al., Proc. Natl. Acad. Sci. USA **107**, 18545 (2010).

[49] R. Milo and R. Phillips, in *Cell Biology by Numbers* (Garland Science, New York, 2015), pp. 209–282.

[50] R. A. Risques and S. R. Kennedy, PLoS Genet. **14**, e1007108 (2018).

[51] M. R. Junttila and F. J. De Sauvage, Nature (London) **501**, 346 (2013).

[52] E. A. Martens, R. Kostadinov, C. C. Maley, and O. Hallatschek, New J. Phys. **13**, 115014 (2011).

[53] M. Schiffman and N. Wentzensen, Cancer Epidemiol. Biomarkers Prev. **22**, 553 (2013).

[54] S. H. Strogatz, *Nonlinear Dynamics and Chaos* (CRC Press, Boca Raton, FL, 2018).

[55] W. Bialek, *Biophysics: Searching for Principles* (Princeton University Press, Princeton, NJ, 2012).

[56] C. W. Gardiner, in *Handbook of Stochastic Methods for Physics, Chemistry and the Natural Sciences*, Third ed. (Springer-Verlag, Berlin, 2004), pp. 117–174.

[57] C. R. Doering, K. V. Sargsyan, and L. M. Sander, Multiscale Model. Simul. **3**, 283 (2005).